



Science Arts & Métiers (SAM)

is an open access repository that collects the work of Arts et Métiers Institute of Technology researchers and makes it freely available over the web where possible.

This is an author-deposited version published in: <https://sam.ensam.eu>
Handle ID: [.http://hdl.handle.net/10985/24883](http://hdl.handle.net/10985/24883)

To cite this version :

Quentin HENRY, Philippe VIOT, Louise LE BARBENCHON, Antonio COSCULLUELA, Jean-Benoit KOPP - Influence of the microstructure on the compressive behaviour of porous aluminas: From microstructural characterisation to fracture mechanisms - Journal of the European Ceramic Society - Vol. 44, n°6, p.4170-4184 - 2024

Any correspondence concerning this service should be sent to the repository

Administrator : scienceouverte@ensam.eu



Influence of the microstructure on the compressive behaviour of porous aluminas: From microstructural characterisation to fracture mechanisms

Quentin Henry^{a,*}, Philippe Viot^a, Louise Le Barbenchon^b, Antonio Coscolluela^c, Jean-Benoit Kopp^a

^a Arts et Métiers ParisTech, Univ. Bordeaux, Bordeaux INP, I2M, UMR 5295, 33000 Bordeaux, France

^b CNRS, Arts et Métiers ParisTech, Univ. Bordeaux, Bordeaux INP, I2M, UMR 5295, 33000 Bordeaux, France

^c CEA-CESTA, 33114 Le Barp, France

ARTICLE INFO

Keywords:

Porous alumina
Microstructural characterisation
Mechanical properties
Compression
Fracture mechanisms

ABSTRACT

The mechanical response of porous aluminas under compressive loading was studied and compared with the fracture mechanisms. Aluminas with a wide range of pore sizes and porosity rates (1–60%) were produced to deconvolve the effects of pore rate, size and morphology on mechanical response. A transition from brittle to quasi-brittle behaviour appears when the porosity rate reaches 60% and a decrease in mechanical properties as the porosity rate increased. At a porosity rate of 20%, a first alumina was produced with micrometric, interconnected pores, while a second was produced with isolated spherical and mesometric pores. The Young's modulus is little affected by pore size and morphology, while failure stress decreases with increasing pore size. At iso-density, different grain arrangements lead to different fracture mechanisms despite a similar mechanical response: the more compact the grain arrangement, the more transgranular the crack propagation.

1. Introduction

High performance ceramics and porous ceramics are characterised by physical properties such as high strength to weight ratio, high hardness, low density and high thermal resistance. These materials are in demand in the energy sector [1] as structural material in nuclear reactors [2] but also in the health sector [3,4]. Aerospace is another important market for advanced ceramics, as they can be used as heat shields in aircraft and rocket engines [5]. Finally, the defence industry is increasingly interested in these materials for armour applications [6,7]. Porous ceramics are valued in a wide range of applications, mainly for their low thermal conductivity [8] and high filtration capacity [9–11]. These materials can also significantly lighten the structures in which they are used. For this reason, and their good mechanical properties in compression, they are being considered for armour applications. However, the characterisation and modelling of the mechanical behaviour of porous ceramics remains a challenge. Given the brittle or quasi-brittle nature of these materials and their great sensitivity to micro- and meso-structural heterogeneities, it is often difficult to predict the emergent mechanical behaviour of these materials without focusing on

the damage and fracture mechanisms that can occur at small scales.

The emergent mechanical response at the macroscopic scale of porous ceramics is strongly correlated with pore rate, pore size and pore morphology. Numerous studies have focused on these different parameters influencing the mechanical behaviour of porous ceramics. Regarding the influence of the porosity rate, several studies show that the Young's modulus (E) [12–17] and compressive fracture stress (σ_f) [10,11,18–20] decrease while the porosity rate increases. Considering the experimental results, several empirical models [12–14,21,22] have been proposed to predict the evolution of Young's modulus and fracture stress as a function of porosity rate without necessarily considering the influence of the size, morphology and orientation of the pores. Although the majority of studies on the mechanical behaviour of porous ceramics focus on the influence of porosity rate, which is generally considered to be a first order influence, there are a few studies in the literature on the influence of pore size and morphology on the mechanical behaviour. Indeed, considering a fixed porosity rate, an increase in pore size generally leads to a decrease in fracture stress [23,24]. However, the wide scatter of results for low porosity levels seems to preclude rigorous conclusions on the effects of pore size [25]. Nevertheless, there are some

* Correspondence to: Institut de mécanique et d'ingénierie, CNRS UMR 5295, Arts et Métiers ParisTech - Campus de Bordeaux, Esp. des Arts et Métiers, Talence 33405, France.

E-mail address: quentin.henry@ensam.eu (Q. Henry).

phenomenological models, notably that proposed by Miled and *al.* [26] to predict the evolution of stress at failure in compression as a function of porosity rate and pore size, considering isolated and spherical pores. This model was compared and validated with results obtained for an inorganic quasi-brittle material. As far as the elastic properties are concerned, there appears to be little work on the influence of pore size on the Young's modulus.

A number of studies have also been carried out on the influence of pore morphology on the mechanical properties of porous brittle materials. The more elongated and interconnected the pores, the greater the reduction in mechanical properties such as Young's modulus and hardness [27,28]. To predict the effect of pore morphology on Young's modulus, simplified homogenisation models or more complex models such as those proposed by Manoloy and *al.* can be used [29], which is an extension of [30,31]. The results of the latter model seem to show good agreement with experimental results obtained on porous ceramics.

Most of the studies described above do not focus on observing damage and fracture mechanisms, which may occur at small spatial scales, in order to explain or predict the results obtained. However, if one wants to improve prediction tools, it seems relevant to try to correlate local mechanisms with macroscopic properties. This is all the more true when the material is complex and the scales of interest are numerous. This is the case for porous ceramics, which are considered to be multi-scale materials, at least in terms of grains and pores scales. Some results are available for brittle porous materials. It is generally accepted that the largest porosity in a brittle material appears to be a precursor site for crack initiation. The experimental work of Sammis and Ashby [32] demonstrates this, later confirmed by several numerical simulations [33]. At the grain scale, observations can vary and depend on numerous parameters (sintering time, porosity rate and size). Intergranular [34] and transgranular [35] failure modes have been observed in several case studies.

Finally, it seems very complex to deconvolve the effects of the microstructure (grain) and mesostructure (pore rate, size and morphology) and to establish a correlation between local damage and fracture mechanisms with the resulting mechanical behaviour. Even if the effect of the size and rate of porosity has been studied for porous ceramics, there is still a lack of understanding allowing to link the influence of porosity on the macroscopic behaviour and the local fracture mechanisms taking place in porous ceramics. The aim of this work is therefore to establish this link between the macroscopic behaviour and fracture mechanisms of porous ceramics and the size and morphology of the pores. In order to achieve this, the choice of the manufacturing process and the type of ceramic produced was strategic. Several porous aluminas (1% to 60% porosity) with controlled pore and grain sizes have been produced using a gel casting process [36]. To highlight the effect of geometry and pore size on mechanical response and fracture mechanisms, two drastically different types of pores were introduced for alumina containing approximately 20% porosity. The first is microscopic and tortuous, while the second is mesoscopic, spherical and isolated. In order to understand their influence on the local fracture mechanisms, the microstructure of porous alumina samples was characterised by electron microscopy and X-ray microtomography before being tested under uniaxial compression. The local observation of the recovered fragments provides information on the fracture mechanisms and will highlight the possible relationship between the fracture mechanisms and the variations in fracture stress.

2. Materials and Methods

2.1. Manufacturing: gel-casting process

Different heterogeneous aluminas were manufactured by the Galtenco Solution company using a gel-casting process [37–39]. Compared to the standard ceramic manufacturing process, a three-dimensional polymer network is created during the gel-casting process. First steps

of the process (steps 1 and 2 in the Fig. 1) consists in mixing a polymeric network (monomer, solvent, cross-linking agent,) with the ceramic powder and pouring it in a mold (step 3 in the Fig. 1). During the step 1 of the gel-casting process, the monomer N,N-dimethylacrylamide (DMAA: C_5H_9NO , stabilized with Mequinol (MEHQ), > 99%, TCI, Japan) and the cross-linking agent N,N-methylenebisacrylamide (MBAM: $C_7H_{11}O_2N_2$, 97%, ThermoScientific, USA) were used in a demineralised water. Ammonium persulfate (APS: $(NH_4)_2S_2O_8$, 98%, Alfa Aesar, USA) was used to initiate the polymerisation at room temperature in the step 2. After the polymerisation of the polymer (steps 4), a wet gelcast sample is first obtained. Dried body was debinded at 600 °C for 1 h under air, with a heating rate of 0.5 °C/min. The debinding cycle was followed by a pre-sintered stage, done in the same furnace, at 1000 °C for 1 h, under air, with a heating rate of 2 °C/min (steps 5 in the Fig. 1) and a sintering cycle at a specific temperature (steps 6 in the Fig. 1) is carried out to give the ceramic its final properties (high strength in compression, high hardness).

A shrinkage phenomenon characterized by a reduction in volume at constant mass due to interatomic diffusion between grains is observed after sintering. The parameters of sintering (temperature T_s and duration t_s) determine the ceramic microstructure. At high sintering time and temperature, the grains will grow and coalesce more [40]. Machining is classically required to obtain the final dimensions. The alumina constitutive powder used in this study is pure at 99.84% but some impurities such as MgO are present in very small quantities (500 ppm). The chemical characteristics of the constituent powder are given in Table 1. The industrial data sheet of alumina powder mentions a median particle size d_{50} equal to 0.44 μm .

First of all, a dense alumina (1% of porosity) was manufactured by sintering during 9 h at 1530 °C (Table 2). This sintering time and temperature lead to significant grain growth, but residual pores remain between the grains. This is why the alumina is not totally dense. This material is considered as the reference. The porosity rate is obtained by comparing the density of the samples with the theoretical density of dense alumina (3960 kg/m^3). Given the presence of porosity, the density is measured using a classic geometric method.

Three different porous aluminas have been produced with two porosity rates and two types of porosity. The first porous shade called 20micro has a porosity rate equal to 21% and contains microporosities between grains induced by sub-sintering [41]. The porosity rate of second shade called 20meso and third shade called 60meso is respectively equal to 22% and 61%. They contain spherical mesoporosities induced by the addition of polymeric preforms during first steps of the process (Table 2 and Fig. 1). These shades are sintered only during 3 h at the same temperature (1530 °C) as for the dense alumina.

The polymeric preforms (isobutane) manufactured by Nouryon are

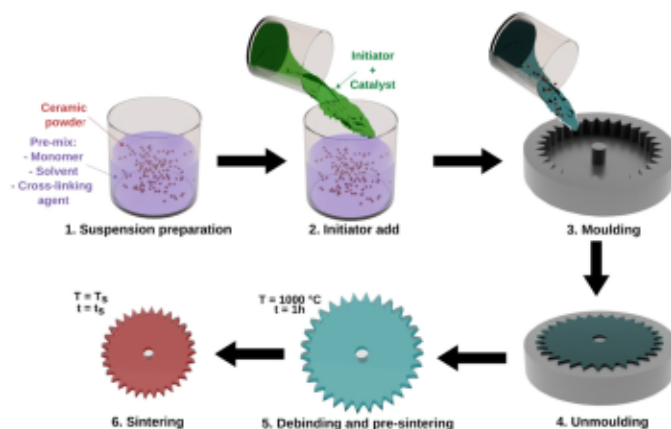


Fig. 1. Gel-casting process consists of six successive steps to manufacture complex shapes in ceramic.

Table 1
Chemical characteristics of alumina constitutive powder (Alteo ®).

Al ₂ O ₃ (%)	Na ₂ O	CaO	SiO ₂	Fe ₂ O ₃	MgO
99.84	400 ppm	240 ppm	295 ppm	180 ppm	500 ppm

Table 2
Manufacturing parameters and characteristics of heterogeneous alumina samples.

Sample	Sintering temperature (T _s)	Sintering time (t _s)	Porosity (-)	Method to introduce porosity	Type of porosity
dense	1530 °C	9 h	0.01 ± 0,01	-	interstitial
20micro	1400 °C	3 h	0.21 ± 0,01	Under sintering	microporosity
20meso	1530 °C	3 h	0.22 ± 0,01	Polymer preforms	spherical mesoporosity
60meso	1530 °C	3 h	0.61 ± 0,01	Polymer preforms	spherical mesoporosity

mainly spheres (Fig. 2.a) and characterised by a d_{50} of spheres diameter between 30 and 50 μm . The diameter distribution of polymeric spheres obtained by a laser profilometer (Fig. 2.b) shows a bimodal distribution. The first main peak (96%) corresponds to the spheres with a diameter between 8 and 100 μm (Fig. 2.a). The second peak is between 0.2 and 0.9 μm but represents only 4% of the polymer spheres. These polymer spheres are introduced during the first steps of the gel-casting process (Fig. 1) with the ceramic powder. During the drying and sintering steps (step 5 and 6 on the Fig. 1), polymeric preforms are pyrolyzed to create spherical pores in ceramic matrix.

2.2. Microstructure observation

As described in the literature, the microstructure such as grain size, pore size and rate have a strong influence on the mechanical response of ceramics [25,42]. It is therefore important to characterise the microstructure in detail using various observation methods, such as scanning electron microscopy (SEM) and X-ray microtomography, in order to detect the most critical pores, which are thought to be responsible for crack initiation.

2.2.1. Scanning Electron Microscope (SEM) observation

A SEM-FEG ZEISS SIGMA 300 was used with secondary electrons and a voltage equal to 15 kV to obtain a topographical information on the surfaces of the samples. The preparation of the samples for SEM observation requires polishing steps up to the use of a diamond solution containing particles of size 0.25 μm . A chemical attack (orthophosphoric

acid during 5 min) followed by a thermal cycling ($T = T_s - 60$ °C during 15 min) was performed to reveal the grain boundaries and thus measure the grain size. The samples were metallized with a gold deposit just before being placed in the SEM. The high resolution of the SEM makes it possible to observe nanometric objects such as the smallest grains or pores (a few nanometres) or dislocation planes on fracture surfaces.

2.2.2. X-ray microtomography observation

SEM allows only to observe porosities on the polished surface. In heterogeneous microstructures such as porous alumina, it is necessary to complete these observations with a volume analysis by X-ray microtomography. A laboratory X-ray microtomograph (GE V|tome|x) was used to observe and analyse mesoporous aluminas. For these observations, a voxel size of 2.72 μm was used in order to observe and analyse almost all the pores of mesoporous alumina.

In order to fully observe the samples in the X-ray beam with a voxel of 2.72 μm , the samples have a square cross-section around $3 \times 3 \text{ mm}^2$ and a height of a few millimetres to make several observations at different heights in one sample. At the end of the scan, around 2020 greyscale images measuring 1803×1851 pixels were created, encoded in 16 bit. Several image processing steps are necessary to analyse these data. Firstly, a thresholding step allows to select only porosities in the matrix (dark grey in the Fig. 3.a). Then a segmentation steps has been applied to separate porosities from each other (Fig. 3.b). In addition, porosities at the edge of the sub-volume are not considered in order to analyse porosities in their entirety. Finally, given that the largest porosities would be the critical defects playing a key role in crack propagation [42] and given the difficulty of isolating the smallest porosities,

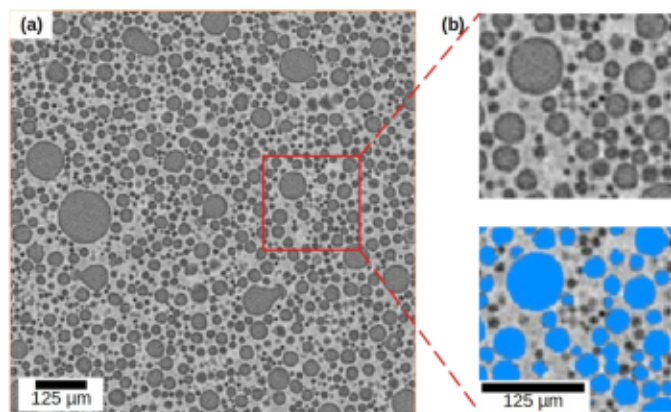


Fig. 3. Raw data in a sub-volume of 1 mm³ (a) and zoom on pores before and after the post-processing steps (b) from X-ray microtomography data of 60meso alumina.

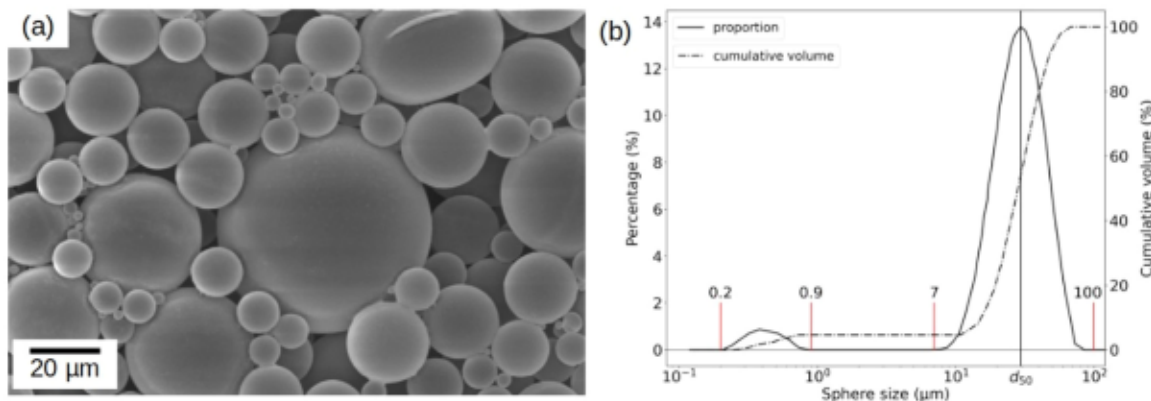


Fig. 2. Pore forming agent: SEM observation (a) and size distribution of polymeric beads (b) manufactured by Nouryon ®.

pores with a diameter of less than $10\ \mu\text{m}$ were not analysed (Fig. 3.b).

A preliminary study showed that a sub-volume size of $1\ \text{mm}^3$ can be considered as a representative elementary volume (REV) containing at least 6 000 pores in 20meso alumina and 19 000 pores in 60meso alumina. In this volume, several porosity parameters are determined as the sphericity, length (maximum of Feret's diameter), volume and barycentre. The sphericity Ψ of a pore is defined as the ratio between the area of a sphere having the same volume that the analysed pore and the area of the analysed pore [43,44],

$$\Psi = \frac{\pi^{1/3} (6V_p)^{2/3}}{A_p} \quad (1)$$

with V_p the volume of analysed porosity and A_p its area. A sphericity equal to 1 means that the pore is perfectly spherical.

2.3. Mechanical characterisation

Quasi-static uniaxial compression tests were performed on a universal mechanical testing machine (ZwickRoell, Z250) coupled with a high-speed camera (Phantom TMX 6410) at a frame rate of 100 000 fps to observe fracture processes during testing. The test is controlled by the displacement of the crosshead. The velocity of the crosshead is $1\ \text{mm}/\text{min}$ which corresponds to a strain rate around $8.3 \times 10^{-4}\ \text{s}^{-1}$. The test is stopped when a sudden drop of 25% of the force is detected. Since alumina is extremely rigid in comparison to the machine, the displacement of the sample is measured locally at its interfaces with punches by a laser extensometer to avoid any error in displacement measurement (Fig. 4.c).

According to the ASTM C1424 norm [45], to avoid any stress concentration, cylindrical samples with a ratio height/diameter equal to 2 ($h = 20\ \text{mm}$ and $\phi = 10\ \text{mm}$) were used. A chamfer of $0.5\ \text{mm}$ was introduced to avoid any initiation of damages at the sharp angle before fracture (Fig. 4.a) [46].

Given that alumina is a very hard material compared to steel used for compression platen of the testing device, the ASTM C1424 norm [45] recommends to place hard punches between the sample and the compression platens. For our study, these compression punches are in tungsten carbide (WC) and their half-diabolo shape allow to ensure a homogeneous stress concentration in the sample. Based on the recommendations given in the standard, the punches were dimensioned using FEM simulation on Abaqus/explicit (Fig. 5). These 2D-axisymmetric FEM simulations were carried out on a quarter of punch/sample assembly by

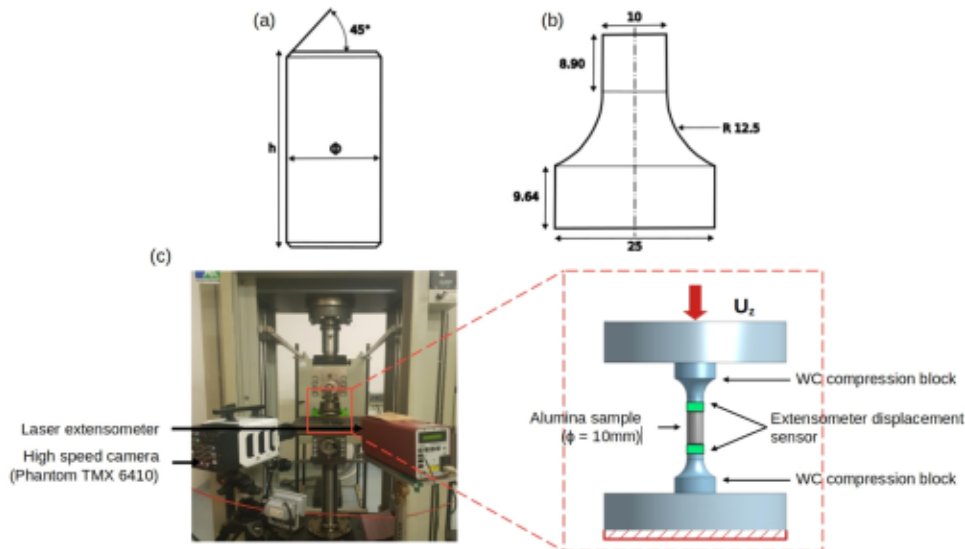


Fig. 4. Cylindrical compression sample (a), Quasi-static compression block in carbide tungsten (b), Quasi-static compression test configuration (c).

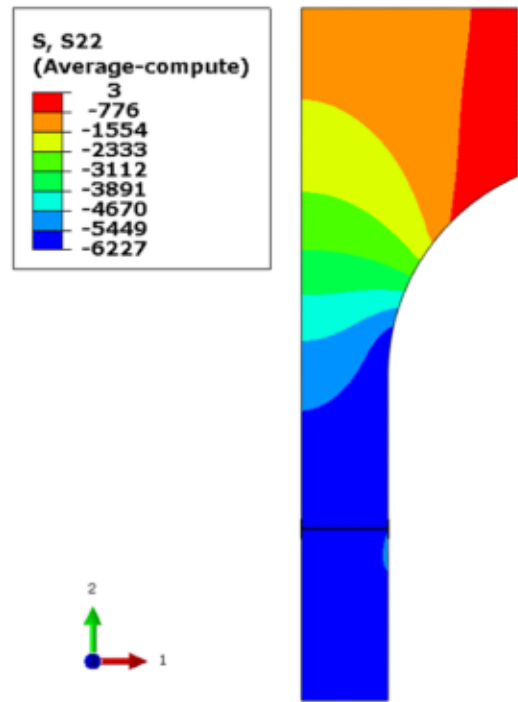


Fig. 5. 2D-axisymmetric FEM simulation (Abaqus/Explicit) of an uniaxial compression test: the colour scale represents the σ_{22} stresses in the punch and the sample.

imposing a displacement of $-0.3\ \text{mm}$ in the vertical direction on the upper face of the punch. The axisymmetry is applied on the vertical axis. The lower side corresponds to the central cross-section of the sample and is blocked vertically and horizontally (Fig. 5). These compression punches have the same diameter as the sample on one side and a diameter of $25\ \text{mm}$ on the other side. As said before, testing without these specific carbide punches can lead to early failure of specimens and therefore obtain much lower compressive fracture stress than expected [47].

From the raw data, the stress σ is determined from the loading force divided by the initial section S_0 of the sample. The strain is calculated from the displacement of the specimen faces measured by the laser extensometer divided by the initial height h_0 . The Young's modulus is

the slope of the linear part of the stress-strain curve (Fig. 6.a) for stress values between 30% and 75% of the maximum stress. The maximum stress (σ_{max}) is the highest stress that can be reached at failure as for 60meso alumina (Fig. 6.b).

For each set of alumina, 10 samples were manufactured and tested. At the end of the compression test, largest fragments are recovered for observation by SEM and X-ray microtomography. These observations allowed the analysis of the cracking paths through the porosities and the understanding of the failure mechanisms that occurred during the failure at a very small scale.

3. Results

3.1. Microstructure characterisation

3.1.1. Qualitative analysis of microstructure by SEM

a) Dense alumina (P = 1%)

The SEM observations of dense alumina show that there are no major defects as lacks of sintering of grains (Fig. 7.a1). Only few small porosities at a nanoscopic scale appear between or within the grains (Fig. 7.a3). A longer sintering time ($t_s = 9 h$) of this grade allows an important coalescence of the grains around the intergranular nanoporosities which can transform some of them into intragranular nanoporosities. For this set, the grain size is determined thanks to the intercept method [48]. It is equal to $1.19 \pm 0.10 \mu m$ and represents an increase of 148% in comparison to the diameter d_{50} of alumina powder equal to $0.48 \mu m$. The coarsening of the grains was expected and is explained by the appearance of physical phenomena (diffusion, atomic rearrangement) which stabilises the energy of the system during sintering [40,49].

b) Microporous alumina 20micro (P = 21%)

There are no major defects in the microstructure of the microporous alumina (Fig. 7.b1 and b2). The SEM observations at a microscopic scale (Fig. 7.b3) allow to observe few microscopic pores which can be considered as residual porosities. For this type of porous alumina, an open porosity rate of $18 \pm 1\%$ was measured by helium pycnometry. Consequently, 85% of the total porosity is open, which proves that the porosity is interconnected and measures only a few micrometres. This result can be attributed to the sintering process being carried out at a lower temperature ($T_s = 1400 \text{ }^\circ\text{C}$) compared to the theoretical temperature required to obtain dense alumina ($1530 \text{ }^\circ\text{C}$). As a result, the grains are unable to grow and coalesce to any significant extent, leading to the persistence of voids between them. For this set, the grain size measured by the intercept method [48] is equal to $0.48 \pm 0.04 \mu m$. In comparison to the d_{50} of the initial powder, the grains of this microporous alumina did not grow during sintering. A similar observation was made in previous studies by Suleiman [41]. However, it is difficult to quantitatively

analyse the size of the porosity based on SEM 2D observations.

c) Mesoporous alumina 20meso (P = 22%)

Mesoporosities can be observed at low SEM magnification (Fig. 7.c1 and c2). An open porosity rate of 1% was measured by helium pycnometry, which corresponds to only 5% of the total porosity rate. These porosities are mainly spherical, closed and isolated due to the porogen shape. The observation of these porosities in 2D shows that they seem to be homogeneously distributed in the material (Fig. 7.c2). The observation of the microstructure at a higher magnification shows that residual porosities between the grains are yet present (Fig. 7.c3). This shade of porous alumina shows a multi-scale porosity with mesoporosities (Fig. 7.c2) and microporosities (Fig. 7.c3). The grain size is equal to $0.81 \pm 0.05 \mu m$, which reflects an increase of 69% of the grain size from the d_{50} of the alumina powder. Indeed, for this grade, a sintering temperature of $1530 \text{ }^\circ\text{C}$ was used, which enables the coalescence and coarsening of the grains to be triggered. However, the sintering duration of 3 h induces only a partial increase in the size of the grains. This lower grain growth explains why there is substantial residual microporosity in the microstructure.

d) Mesoporous alumina 60meso (P = 61%)

The pores of the alumina with 61% of porosity are mainly spherical. High magnification SEM observations (Fig. 7.d2) show that some of them are interconnected. Indeed, due to the high porosity rate, the mesopores are close to each other, inducing interconnections between the closest pores. An open porosity rate of 12% was measured by helium pycnometry, which corresponds to only 20% of the total porosity rate. This may be due to the high proximity of the polymeric spheres to each other which prevents the ceramic grains from slipping between them during the first step (suspension preparation) of the process (Fig. 1). Indeed, the distance between two spheres may be less than the diameters of the ceramic grains, so they cannot penetrate between the spheres, leaving a void and therefore a hole between two porosities at the end of the drying stage as represented in Fig. 8.a and observed in Fig. 8.b. These holes can also form during the high-temperature sintering step, which renders the thin walls brittle due to shrinkage. The observation of the microstructure at higher magnification shows that residual porosities between the grains are present (Fig. 7.d3). The 60meso alumina set also exhibits a multi-scale porosity with mesoporosities and microporosities. The grain size of this shade is equal to $0.70 \pm 0.04 \mu m$. The grain size of 60meso alumina is similar to that of the 20meso alumina because the same sintering conditions (time and temperature) were used.

These initial observations of the microstructure show that the size and shape of the pores depend on the method used to introduce them. Their size ranges from a few micrometres with the sub-sintering method to $200 \mu m$ with the use of polymeric spheres. Grain size is also affected by the parameters of the manufacturing process. A long sintering time at high temperature can double the initial grain size. Lower temperatures

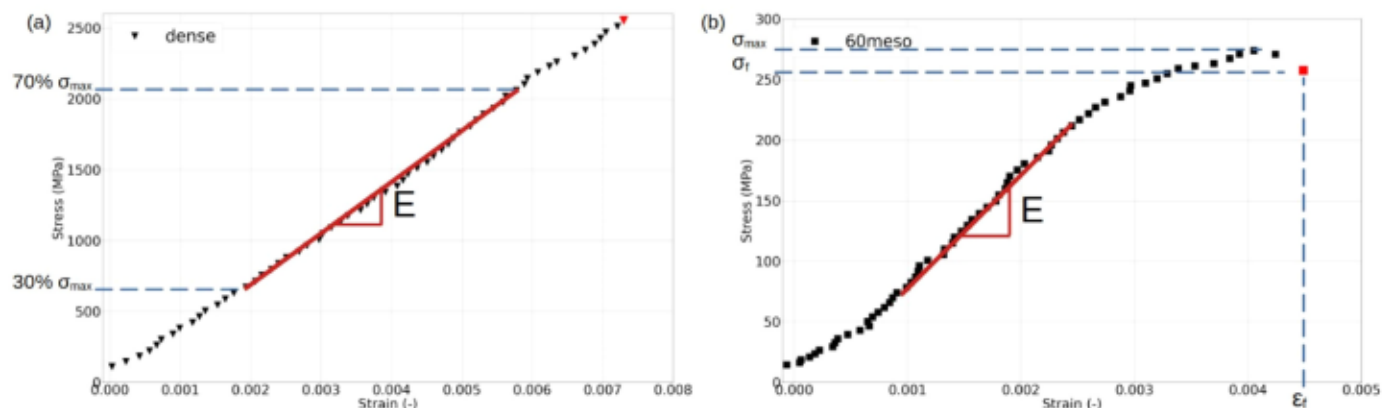


Fig. 6. Determination of the Young's modulus and fracture stress thanks to the stress/strain curve of alumina with an elastic brittle behaviour (a) and non-linear brittle behaviour (b).

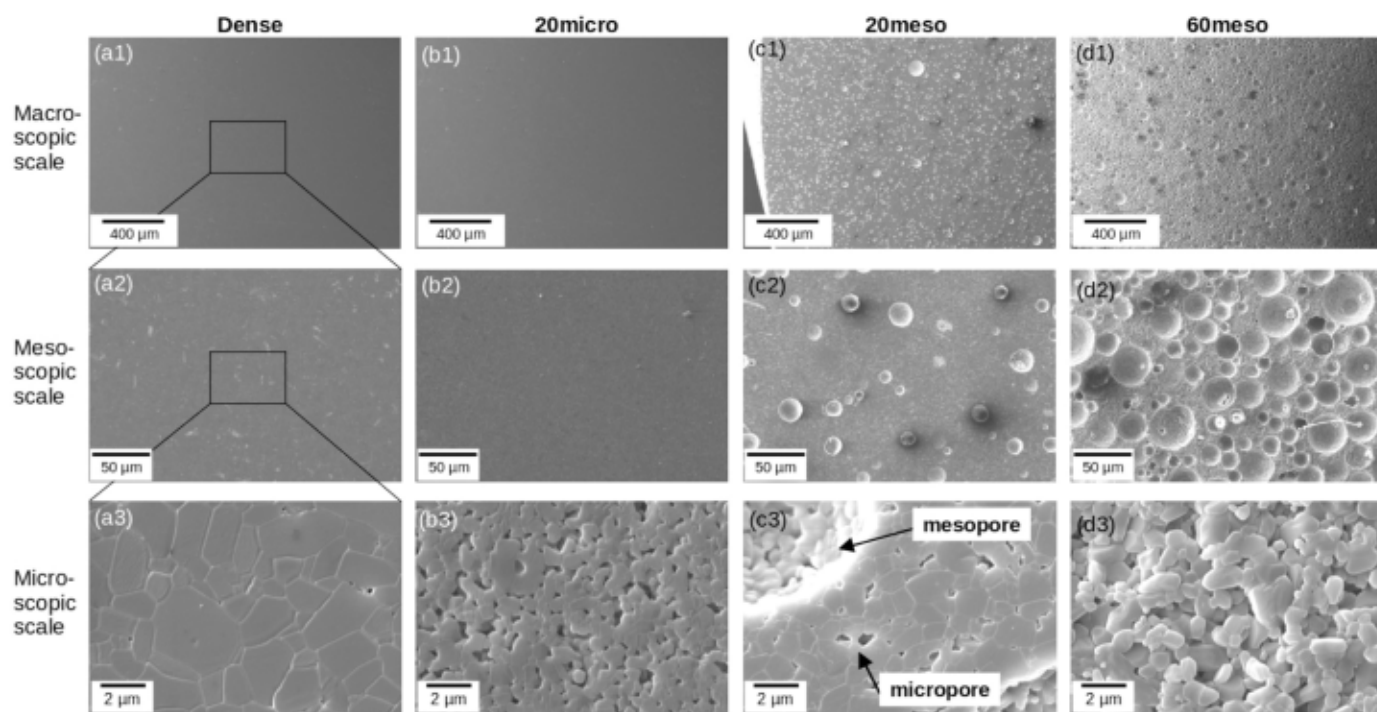


Fig. 7. Scanning electronic microscopy (SEM) observation of the microstructure of dense (a), 20micro (b), 20meso (c) and 60meso alumina (d). The figures in the second row (X1000) are a magnification of the figures in the first row (X100) and similarly the third row (X20 000) is a magnification of the second row.

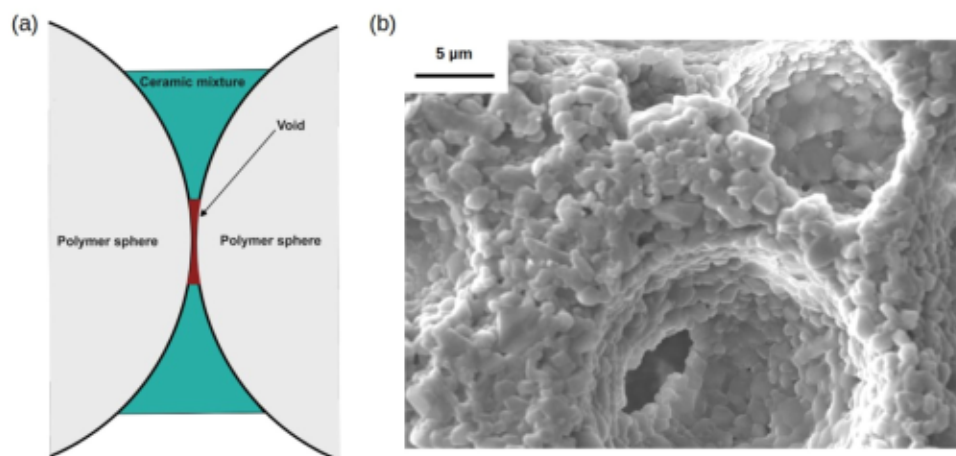


Fig. 8. Schematic representation of grains blocked by closely spaced polymer spheres (a), SEM observation of a hole between two pores X5000 (b).

and shorter sintering times result in limited grain coalescence and growth. As a result, residual porosities are left within the microstructure.

3.1.2. Quantitative 3D analysis of microstructure of mesoporous alumina

a) Volumic reconstruction of porosities

The volumic reconstruction of microtomography raw data allows to observe the morphology of pores in 3D and their arrangement in the volume. As mentioned above, due to the voxel size ($2.72 \mu\text{m}$) used, which is on the order of micropore size, it is impossible to analyse this type of porosity. This is why 20micro alumina was not analysed by X-ray microtomography in this section.

The volume reconstruction of raw data of 20meso alumina shows that porosities seem to be well isolated and spherical (Fig. 9.A.i). On the contrary, the volume reconstruction of the 60meso alumina raw data

(Fig. 9.B.i) shows that some pores can have a more complex and elongated shape (detailed in Fig. 9.B.i) and the pores seem to be closer together. Thanks to post-processed data, it is possible to only represent porosities and classify them by their diameter as in Fig. 9.A.ii and B.ii. It seems that a majority of pores has a diameter lower than $75 \mu\text{m}$ for both mesoporous alumina (20meso and 60meso). It also appears that few pores have a diameter larger than $200 \mu\text{m}$ as shown in Fig. 9.A.iii and B.iii which represent only pores with a diameter larger than $49 \mu\text{m}$.

b) Distribution of sphericity and diameter

For the 20meso alumina, the distribution of sphericity indicates that 95% of porosities have a sphericity greater than 0.9. the peak of sphericity distribution shows that 65% of the studied pores have a sphericity of 1, which proves that the porosities are mainly spherical (Fig. 10.a). Porosities with a complex shape can reach a sphericity of 0.5 (Fig. 10.b).

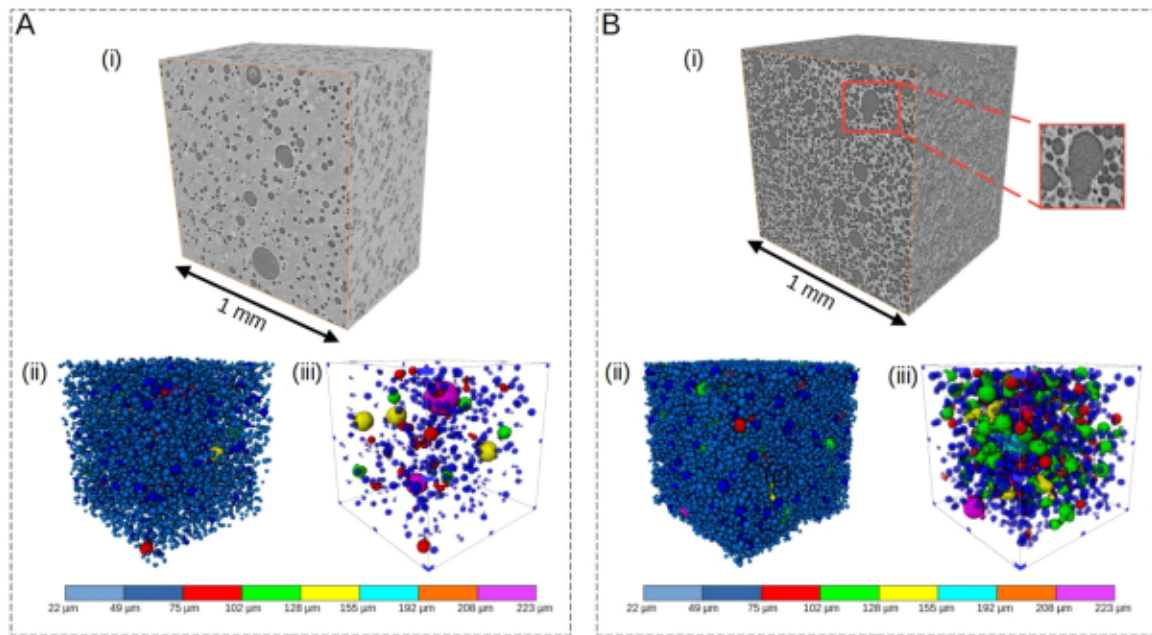


Fig. 9. Volume reconstruction of 20meso (A) and 60meso (B) of the raw data (i), all porosities (ii) and porosities with a diameter higher than 49 μm (iii).

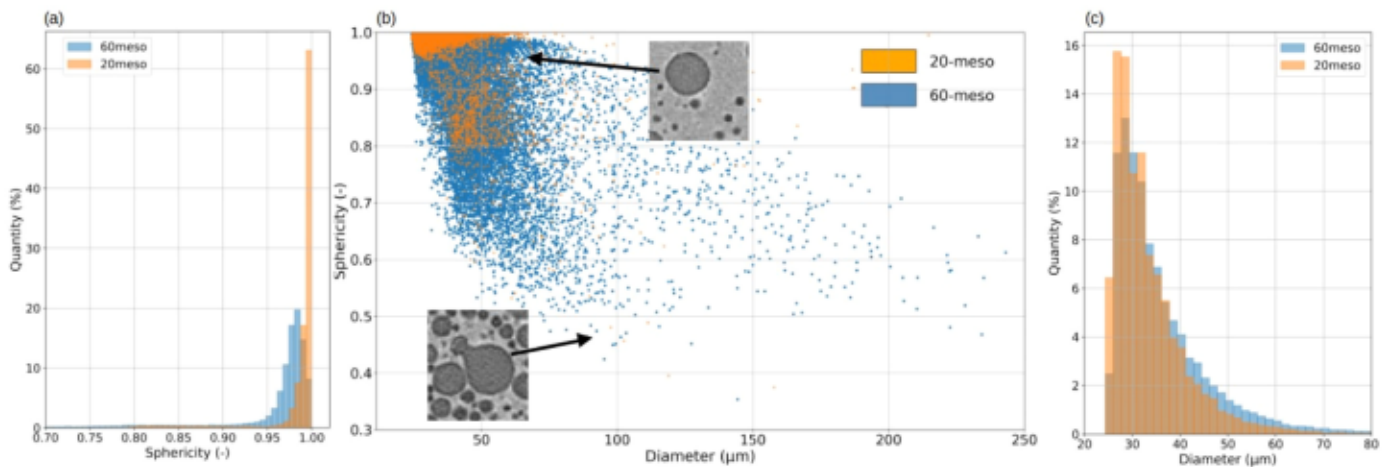


Fig. 10. Distribution of sphericity (a), distribution of diameter (b) and sphericity versus diameter (c) of 20meso (blue) and 60meso (orange) alumina.

The deviation from perfect sphericity is mainly due to interconnected pores. The size distribution of the porosities shows that the majority of porosities has a maximum length lower than 75 μm (Fig. 10.c). Moreover, some porosities have a diameter between 100 and 250 μm (Fig. 9.A.iii). These very large porosities may be privileged places of initiation for cracks during mechanical tests as explained by Rice [42]. The graph (Fig. 10.b) represents the transition of the sphericity as a function of the diameter. The 20meso alumina have mainly spherical ($\Psi > 0.9$) and small pores but there are also few large pores with a sphericity value lower than 0.6.

For 60meso alumina, the sphericity distribution shows that the porosities are essentially spherical (Fig. 10.a). However, the peak of sphericity distribution shows that only 20% of the studied pores have a sphericity of 1 and the sphericity distribution around the peak is wider. Indeed, there are less pores (87,3%) with a sphericity greater than 0.9 compared to 60meso alumina (95%).

This proves that pores of 60meso alumina present a more complex morphology than those of 20meso alumina while the same spherical polymer spheres were used as pores forming agents. Moreover, we notice that the sphericity values can reach 0.6 for some porosities. This

wider range of sphericity values shows a part of 60meso alumina porosities have morphologies far from that of a perfect sphere. As explained above, this is reflected in the great proximity of porosities which lead to the formation of holes inside walls between porosities. The size distribution of the porosities of 60meso alumina shows that the majority of porosities have a maximum length lower than 75 μm and it is possible to observe porosities which maximum length exceeds several hundred micrometers (Fig. 9.B.iii).

For 60meso alumina, the Fig. 10.b shows that small pores are also predominantly spherical but there is a larger number of large pores with a sphericity much lower than 1. In both mesoporous alumina (20meso and 60meso), these large porosities with a complex geometry could be ideal candidates for crack initiation [42].

3.2. Mechanical characterisation under compression loading

3.2.1. Macroscopic mechanical behaviour in compression

The stress-strain response of dense and porous alumina under uniaxial compression is shown in the Fig. 11. The linear stress-strain behaviour of dense and 20% porous alumina is typical of elastic brittle

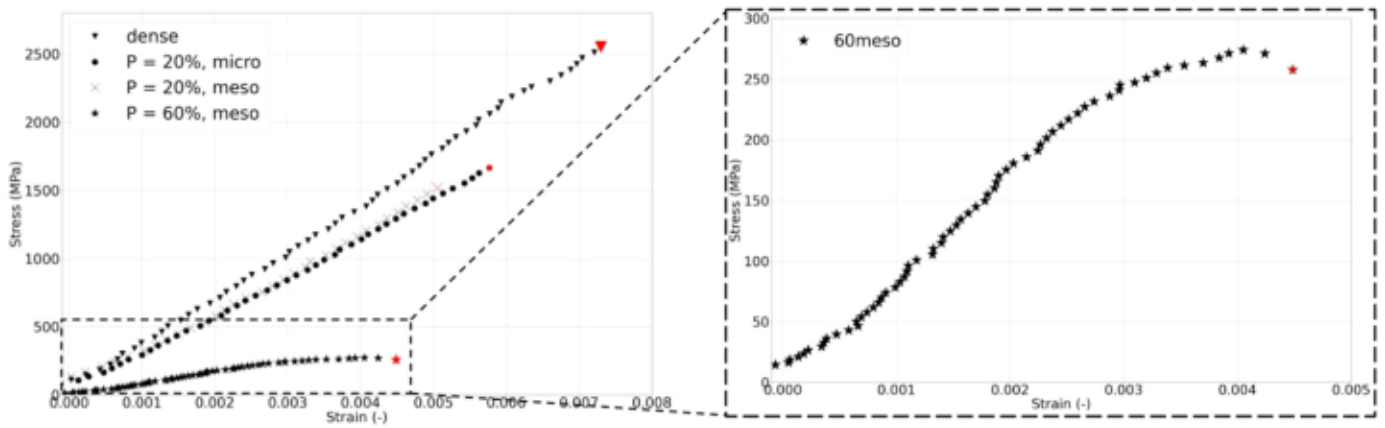


Fig. 11. Stress/strain curves for the different shades of alumina tested under uniaxial compression. The red point at the end of the stress/strain curves matches with the fracture of the samples.

material ($\sigma_{max} = \sigma_f$). For the most porous alumina (60% of porosity), the stress-strain curve is characterised by firstly a linear zone and secondly by a beginning of non-linearity (damage plateau) just before the fracture that leads to fracture stress σ_f less than the maximum value of stress σ_{max} .

These mechanical responses are characteristic of a quasi-brittle behaviour and highlight the Young's modulus and fracture stress are higher for dense ceramic than for porous alumina (Table 3). The Young's modulus decreases from 366 ± 88 GPa for dense alumina to 64 ± 12 GPa for 60meso alumina and the fracture stress drops from 2536 ± 396 MPa to 209 ± 22 MPa. For alumina grades with 20% porosity (20micro and 20meso), no significant difference is noticed concerning the mechanical response despite very different size and type of porosity (microporosity and mesoporosity). Only, the fracture stress is slightly lower for 20meso alumina (1038 ± 147 MPa) than for 20micro alumina (1252 ± 115 MPa). The pore size may explain this variation. In addition, a large dispersion of values of fracture stress and Young's modulus are observed for dense and 20% porous aluminas typical of brittle fracture [25,50]. For 60% porous alumina, the dispersions are smaller with the development of damage of the material leading to the propagation of a single macro-crack.

This change of mechanical behaviour in compression as been observed by Meille *et al.* for a porosity rate around 50% [25]. For brittle aluminas, mechanical properties are controlled by the presence of critical isolated pores. While for quasi-brittle alumina, the mechanical response is driven by the progressive damage of the walls between the pores. For low porosity, the compressive stress-strain curve is typical of brittle behaviour with the propagation of a few long cracks, parallel to the loading direction. Compressive fracture of low porosity ceramics has been described in the literature [32,51]. Cracks initiate from the largest porosities parallel to the applied load and propagate in a stable manner as demonstrated for a perforated 2D plate in brittle polymer material. Finally, interactions between cracks lead to the final failure of the sample. For a highest porosity rate, after the initial linear zone, the

Table 3

Young's modulus and fracture stress determined by quasi-static uni-axial compression tests.

Sample	Young's modulus E (GPa)	Fracture stress (MPa)	Porosity (-)	Number of sample
dense	366 ± 88	2536 ± 396	0.01 $\pm 0,01$	4
20micro	232 ± 16	1252 ± 115	0.21 $\pm 0,01$	10
20meso	227 ± 34	1038 ± 147	0.22 $\pm 0,01$	10
60meso	64 ± 12	209 ± 22	0.61 $\pm 0,01$	10

non-linearity of stress strain curve can be due to a progressive damage of the solid phase by micro-cracking from pores.

3.2.2. Analyse of sample fracture

The fracture behaviour of all alumina grades remains brittle, with a significant drop in stress. In particular, the fracture appears more explosive for certain grades, such as dense, 20micro, and 20meso alumina, leading to the creation of several fragments. The fragments recovered after a quasi-static compression test depend a lot on the grade of alumina tested.

For dense alumina, the 20micro and the 20meso grade, the failure is explosive as the Fig. 12.a shows it.

The specimen explodes into small powder-like fragments as Brannon also observed on dense SiC ceramics [52]. The recovered fragments measure only few millimetres for the largest ones and do not have a specific shape (Fig. 13.a, b and c). For the grades with purely elastic behaviour (dense, 20micro and 20meso), many defects are activated during the loading. Considering the high level of loading reached, a high quantity of energy is stored. Thus, at the point of failure, all the energy is released during cracks initiation and their propagation. It could explain the multi-fragmentation of the sample as well as the explosive behaviour. The third and the fourth frames of Fig. 12.a show emission of visible light from the bottom of the specimen. This emission of light during the fragmentation of the specimen can be associated with the conversion of the energy of the mechanical shock into light (triboluminescence) as explained by Brannon [52].

On the contrary, for the 60meso grade, the damage process is progressive (Fig. 12.b). Because, as shown in Fig. 13.d, the sample retains its initial shape and only few macroscopic cracks propagate from both side of the sample and parallel to the direction of applied stress. In fact, the non-linearity of stress/strain curve is due to a progressive damage of the solid phase between pores which occurs by tensile cracking either through bending of the walls. It could explain the non-explosive nature of the failure [1,25]. The decrease in stiffness corresponds to the stable propagation of these cracks. Their coalescence produces instability and the final failure of the sample. The analysis of the images obtained by high-speed camera shows that the fracture of the sample depends on the microstructure.

3.2.3. Observation of post-mortem samples

Surfaces of fragments retrieved from uniaxial quasi-static compression test were observed with SEM and X-ray microtomography in order to determine locally the failure mechanisms (i.e cleavage, transgranular or intergranular mode) (Figs. 14 and 15).

The fracture surface of the dense alumina at low magnification (X 500) does not show any defects at this scale (Fig. 14.a1). But

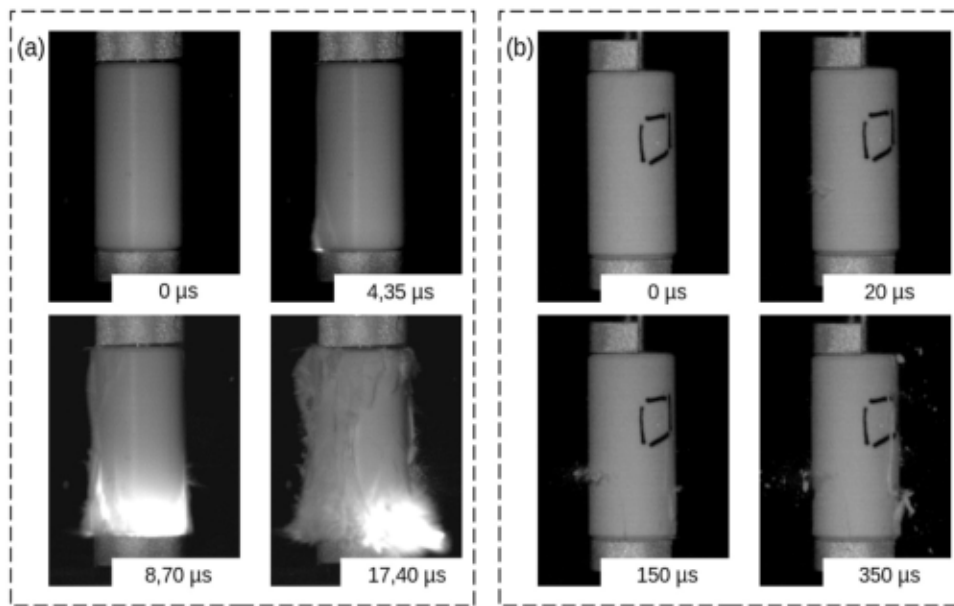


Fig. 12. Fragmentation of sample during a quasi-static compression test: Explosive behaviour of dense alumina (a), non-explosive behaviour of 60meso alumina (b).

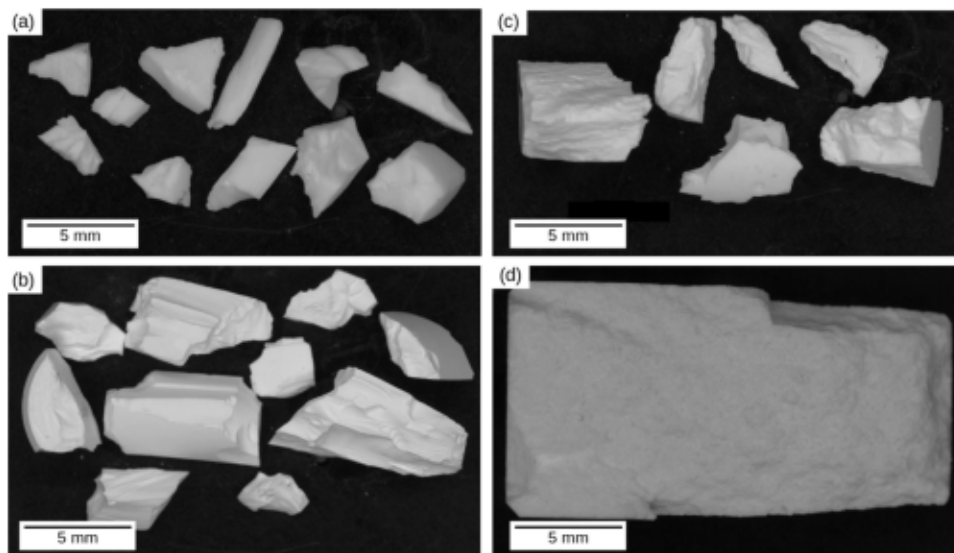


Fig. 13. Fragments of alumina sample after a quasi-static compression test on (a) dense, (b) 20micro, (c) 20meso and (d) 60meso alumina.

observations at higher magnification (X 20 000) reveal cleavage zones (in blue in the Fig. 14.a2) as well as flat grains which are indicators of a mainly transgranular fracture [34]. In addition, it is possible to observe intragranular porosities as explained in the Section 3.1.1. These nanoporosities can be considered as critical defects and therefore as preferential sites for crack initiation for the dense alumina.

In the Fig. 14.b1, the fracture surface of 20micro alumina shows a relative roughness of the fracture plane with macrocracks highlighted (in red dash line). The magnified view (Fig. 14.b2) of this alumina grade shows a roughened appearance of the fracture surface. The shape of the grains is well defined (Fig. 14.b3), as in the microstructure characterisation (Fig. 7.b3), suggesting that the fracture is predominantly intergranular [41]. For few grains, it is possible to observe cleavage zones on the surface representative of a transgranular fracture but these zones remain in minority (Fig. 14.b3).

Concerning mesoporous aluminas, at large scale, macrocracks deflection due to pores are observable at the surface of 20meso

alumina's fragments (Fig. 14.c1) but also inside fragments (Fig. 15). The surface seems to be rougher than for 20micro alumina mainly due to the pores. At a lower scale (Fig. 14.c2), the morphology of grains is well defined indicating intergranular fracture but some zones of cleavage (blue arrow) and flat grains (green dash line) are also present on the fracture surface which is evidence of transgranular fracture. Furthermore, fracture surface showing cracks propagating with a mixed-mode of intergranular and transgranular fracture and some pores blocked inside pores are observed (orange arrow).

For the last grade 60meso alumina, the surface aspect is very rough due to the presence of a high porosity rate (Fig. 14.d1). More extensive damage is observed in this microstructure. This damage takes the form of microcracks in the walls between the pores and macrocracks propagating between the pores (red dash line). Using numerical simulations, Deshpandes and Piat [33] demonstrates that for high levels of porosity (>60%), the damage is distributed throughout the volume of the sample. The fracture seems to be mainly intergranular because the grains are

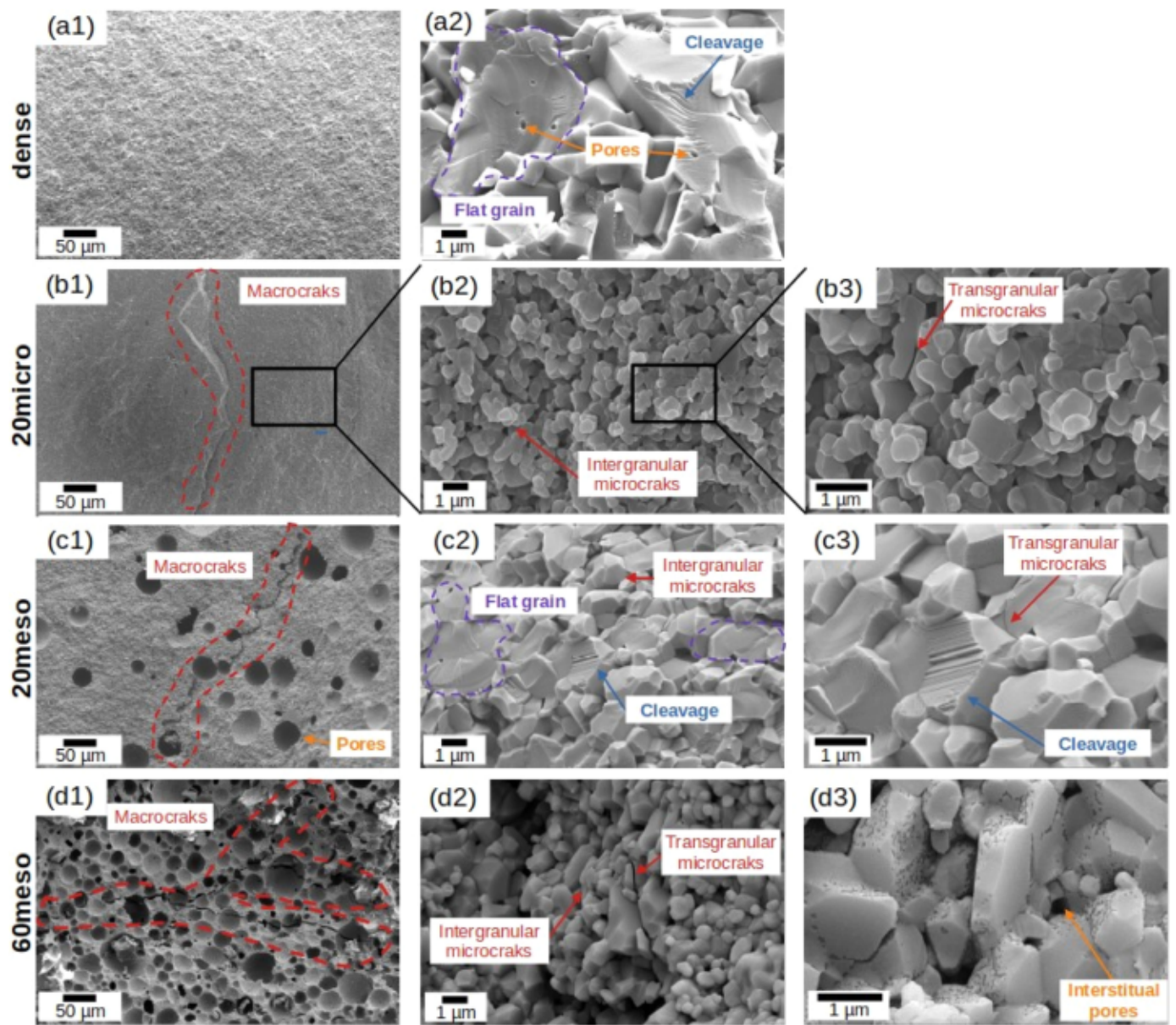


Fig. 14. SEM observations showing the fractography of samples under quasi-static loading at different scales: dense (a1), (a2), 20micro (b1), (b2), 20meso (c1), (c2) and 60meso alumina (d1), (d2). The figures in the second column (X20 000) are a magnification of the figures in the first column (X500) and similarly the third column (X40 000) is a magnification of the second column.

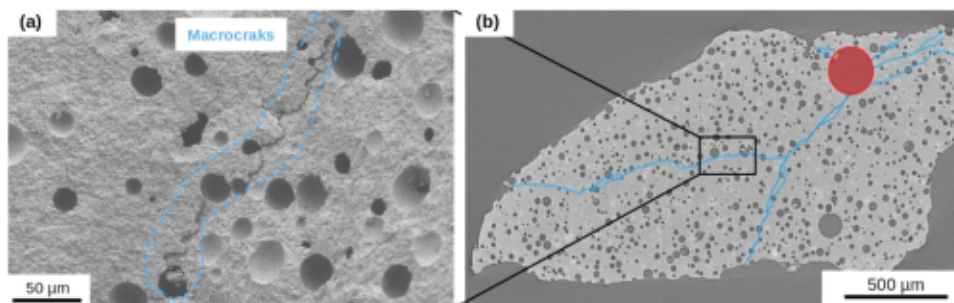


Fig. 15. X-ray microtomography observation of 20meso post-mortem sample after quasi-static loading.

intact at the fracture surface (Fig. 14.d2). Nevertheless, some grains present a transgranular fracture (red arrow) but this mechanism stays in minority.

Unlike SEM observations, which only show the surface of fragmented samples (Fig. 15.a), X-ray microtomography observations of a 20meso post-mortem sample (Fig. 15.b) allow to observe multiple cracks within

the sample itself. This image shows that the largest pore (in red in the Fig. 15.b) plays an important role in ceramic fracture [42], since a multitude of cracks (in blue) interact with it. These observations are in agreement with the numerical results obtained by Deshpandes and Piat [33] on artificial 3D microstructures. For a porosity of the order of 20% and for a mesopore distribution equivalent to that of 20meso alumina, cracks propagate from pore to pore along a preferential path. However, it is still difficult to say whether cracks initiate from these large defects or whether they stop there. It seems that they act as preferential sites for crack initiation, as crack opening is larger near the largest porosity [42]. Moreover, the cracks (in blue) can divide into several branches, which can be explained by the presence of a specific arrangement of pores leading to the cracks branching.

4. Discussions

Previous results have shown that the microstructure (type, size and rate of porosity) generates different behaviours at a macroscopic scale. These variations can be observed through the variation of Young's modulus and fracture stress as a function of the porosity rate at a macroscopic scale. At the microscopic level, fracture mechanisms are also modified by the microstructure of the aluminas studied.

4.1. Influence of the porosity rate on the Young's modulus

As it is shown in the Fig. 16, the Young's modulus is highly dependent on porosity rate. It decreases exponentially with increasing porosity. Comparison with these results from the literature [12,53,54] shows that the variation in experimental Young's modulus data obtained in this work follows the same trend as those in the literature (Fig. 16) for alumina and other sintered ceramics. Moreover, for alumina grades with 20% porosity, no difference is observed experimentally despite the different types of porosity (microporosity and mesoporosity) as the macroscopic behaviour in Fig. 11 suggested. The standard deviation is however more important for the 20meso alumina.

4.1.1. Empirical models

The variation of the Young's modulus as a function of porosity can be represented by different empirical models [12,13,53]. One of them has been developed by Phani and Niyogi. This polynomial equation represents variations in Young's modulus as a function of porosity rate [53],

$$E = E_0(1 - aP)^n \tag{2}$$

where the material constant a may be defined as the packing geometry factor, with a value lying between 1 and 3.85 [53]. The second material constant n is dependent of pore geometry and grain morphology. The n values increased from 2.14 for closed spherical pores, to 4.12 for interconnected pores of irregular shape for porous alumina [53]. There is no limitation in the range of porosity for the validity of the Phani's equation [53]. For Phani's law (Fig. 16, black line) the constant $a = 0.84$ and the material constant $n = 2.46$ have been determined with the experimental data of dense alumina, 20meso and 60meso alumina. These values are very close to the Phani's value [53] for spherical and isolated pores that prove this law represents well the variation of Young's modulus versus porosity. A correlation factor of 0.999 was calculated for this law.

4.1.2. Analytical models of Young's modulus

Several analytical models are used to predict the Young's modulus of porous ceramics. As explained by Buncianu et al. [10] and detailed in numerous papers of Pabst et al. [17,55,56], to estimate the Young's modulus (E) with the following models, the first steps are to calculate bulk (K) and shear (G) modulus for each model and use them in the elasticity standard equation (Eq 3)

$$E = \frac{9KG}{3K + G} \tag{3}$$

The equations obtained by these steps representing the variation in Young's modulus as a function of the porosity rate for three models are written in the following Table 4. Hashin-Strinkman proposed an upper bound model dedicated to macroscopic isotropic two-phased composite [57]. In the case of porous material, pores are considered as material with a zero rigidity. The variation of the Young's modulus with the porosity rate is given by the equation (a) in the Table 4 for isotropic

Table 4
Analytical predictions of Young's modulus.

Models	Hashin-Strinkman upper bounds[57]	Power law - Pabst [55,56]	Exponential law - Pabst[55,56]
Equations	$E_{HS} = E_0 \frac{1-P}{1+P} \quad (a)$	$E = E_0(1 - P)^{(b)}$	$E = E_0 e^{-P} \quad (c)$

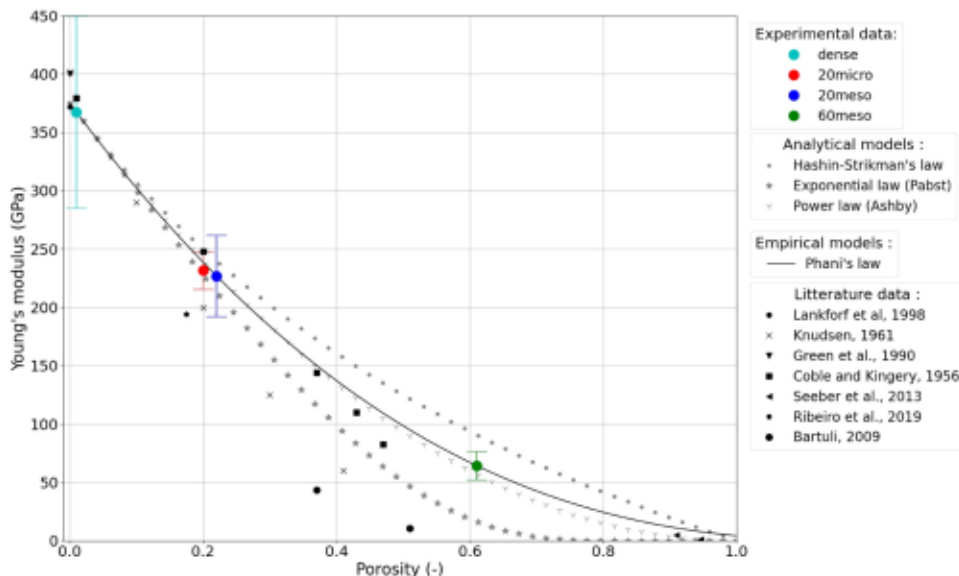


Fig. 16. Effect of porosity on the Young's modulus.

material with a Poisson's ratio equal to 0.2. There are also two significant non-linear models that do not violate the Hashin-Strinkman upper bounds. The first is an exponential relation proposed by Pabst *et al.* [55, 56] to represent the variation of Young's modulus with porosity rate (equation (b), Table 4). The second law proposed is a power relation (equation (c), Table 4). For those equations, P represents the porosity rate.

These two non-linear expressions take into account an adjustable fitting parameter $[E]$ which depends on the Poisson's ratio ν [55,58]. The variations of this parameter $[E]$ as a function of the Poisson's ratio in the range [0.18 - 0.3] (Table 5) shows that the parameter $[E]$ remains constant and equal to 2 in this range.

$$[E] = \frac{3(1 - \nu)(9 + 5\nu)}{2(7 - 5\nu)} \quad (4)$$

It is widely acknowledged in the literature that the Poisson's ratio for dense alumina is approximately 0.22 [10,56]. Zivcova *et al.* [56] demonstrated that the Poisson's ratio remains close to 0.22 in the 0–40% porosity range and decreases slightly to 0.18 in the 40–60% porosity range for alumina. However, according to the previous table (Table 5), the value of fitting parameter $[E]$ will be taken to be equal to 2 despite a reduction in the Poisson's ratio over the 0–60% porosity range.

With a fitting parameter equal to 2, the equations in Table 4 are now written as follows:

- Exponential law:

$$E = E_0 \exp\left(\frac{-2P}{1-P}\right) \quad (5)$$

- Polynomial law:

$$E = E_0(1 - P)^2 \quad (6)$$

For the former relation (Eq. 5), good agreement has been obtained with experimental data for several porous ceramic materials (alumina, zirconia, silicon carbide and silicon nitride) exhibiting a maximal pore volume fraction of about 53% [55]. The latter (Eq. 6) can be obtained from the Gibson-Ashby approach for open-cell foams, based on the concept of a structure composed of solid struts whose mechanical behaviour is governed by the combined effects induced by their bending and tension during a macroscopic compression test [10,59,60].

For a low porosity rate (lower than 0.2), all models give similar results (Fig. 16). Young's modulus of dense, 20meso and 20micro alumina are close to values predicted by these three models. However, it seems that experimental data are closer to value predicted by the power law. For higher porosity rate and especially for $P = 60\%$, value predicted by the exponential law (Eq 5) and by Hashin-Strinkman upper bound are far from the experimental value. Only the polynomial law (Eq. 6) predicts a correct value for the Young's modulus, with a deviation of 4.3 GPa from the experimental value. This deviation is less than the dispersion of the results for the porosity rate considered ($P = 60\%$). The Young's modulus values of porous aluminas determined in a uniaxial compression test can be estimated by a power law over the entire porosity range despite the fact that the model is adapted to cellular materials [59,60].

4.2. Influence of porosity rate on the ultimate strength in compression

It has been observed that mechanical properties can be affected by grain size. Indeed, the larger the grain size, the lower the fracture stress

Table 5
Variation of the fitting parameter $[E]$.

ν (-)	0.18	0.20	0.22	0.24	0.26	0.28	0.3
$[E]$ (-)	1.996	2	2.003	2.005	2.006	2.006	2.005

[19,61,62]. Zimmerman *et al.* [63] have shown that below $5 \mu\text{m}$, the grain size has no influence on the fracture stress. In this study, for the dense and porous aluminas, the average grain size is small and well below $5 \mu\text{m}$ so it can be considered as a second order parameter after the porosity.

Several references [21,25] demonstrate that the ultimate fracture stress in compression is highly dependent on porosity (Fig. 17). The compressive fracture stress decreases exponentially with the increase in porosity, as shown by Grigor'ev [54] and Meille *et al.* [25] in their work. From the equation linking the Young's modulus to the porosity rate of Wagh *et al.* [64] and taking into account energy considerations related to Griffith's theory [65], it is possible to link the fracture stress with the porosity rate by the equation

$$\sigma_f = \sigma_0(1 - P)^n \quad (7)$$

where σ_0 is fracture stress in compression for fully dense alumina, P is the porosity rate and n a empiric constant. This equation has been well detailed by Staub [1] and used on ceramic superconductors by Tancret *et al.* [21]. It is similar to Phani's equation for the variation of Young's modulus considering the constant $a = 1$. The experimental data of fracture stress plotted against porosity fits well with this equation with a constant n equal to 3.73. A correlation factor equal to 0.994 has been calculated that proves this law represents well the variation of fracture stress against porosity.

In addition, as for Bartuli [66] and Meille [25] in their works, the relative standard deviation increases as the porosity rate decreases due to the brittle behaviour of alumina. Indeed, Lamou has explained [50] the relative standard deviation reflects the difference in size of the critical defects in each specimen. For a given stress level, failure (crack initiation and propagation) is determined by the probability of finding a critical defect. The lower the porosity rate, the lower the probability to find a critical defect, therefore the measurement dispersion decreases.

Furthermore, at iso-density, experimental fracture stress is higher than those obtained from literature data. These differences could be explained by the size of pores. Indeed, the pore size has a strong influence on the variation of the fractures stress as Yoshida showed it [24]. At iso-density, the smallest the porosities, the higher the fracture stress.

4.3. Influence of pore size on mechanical properties in compression

As for the rate of porosity, the size of pores may have a strong effect on the mechanical properties of ceramics. For a low porosity rate ($\approx 20\%$), it seems that the fracture stress is slightly lower for alumina with the largest pores (20meso: $\sigma_f = 1038 \pm 147$ MPa) than for the smallest pores (20micro: $\sigma_f = 1252 \pm 115$ MPa). The increase in average pore size from $0.5 \mu\text{m}$ (20micro) to $33 \mu\text{m}$ (20meso) results in a 17% reduction in fracture stress in compression. The scatter of experimental data are close for the two shades of porous alumina, which makes it difficult to conclude on the effect of pore size on these properties. This trend has been also observed by Meille *et al.* [25]. It has been observed that pore size have a strong influence on the mechanical properties: the larger the pore size, the lower the fracture stress [24,25]. This variation could be represented by an inverse law [24]. Meille *et al.* [25] studied porous aluminas with two distinct pore sizes. A first batch of porous alumina were manufactured with spherical pores and characterised by a pore diameter lower than $125 \mu\text{m}$. The second batch is characterised by a pore diameter between 224 and $335 \mu\text{m}$. For a porosity rate equal to 60%, the fracture stress of these porous aluminas decrease respectively from 62 ± 6 MPa to 38 ± 5 MPa.

By applying Miled's model to the microstructures observed in this study, the increase in fracture stress in compression between 20meso and 20micro alumina can be explained by the decrease in pore size. Three parameters can play a role in the mechanical response in compression: morphology, pore size and pore distribution. In the case of low-porosity ceramics, the wide dispersion of the results, characteristic

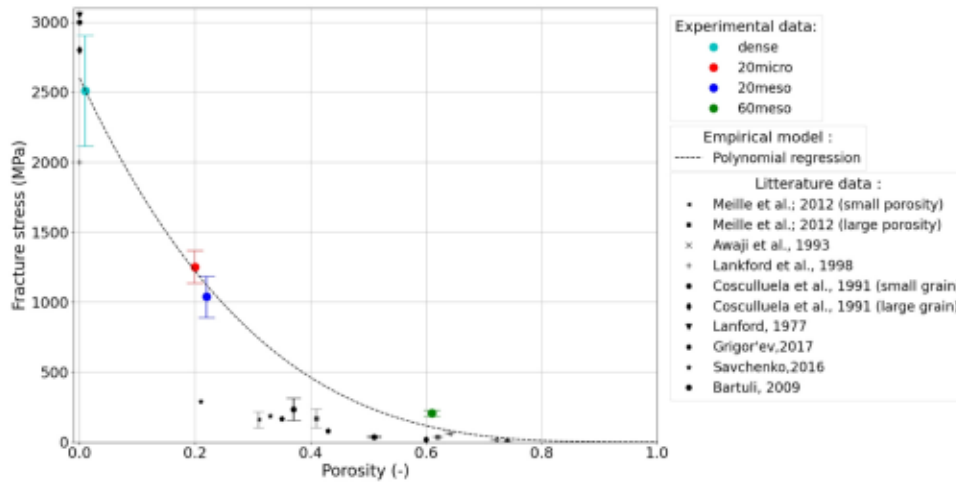


Fig. 17. Effect of porosity on the fracture strength in compression.

of brittle behaviour, may mask the possible influence of pore size [25]. However, Miled et al. [26] proposed a phenomenological model to predict the strength $\sigma(p, \phi)$ as a function of porosity rate p and porosity size ϕ considering spherical pores. This model has been confirmed with experimental data for porosity rates less than 50%. For example, an increase of pore size from 1 mm to 6.3 mm leads to a 44% reduction of the fracture stress in compression. The phenomenological model proposed by Miled is detailed in the appendix A.

In the case 20micro alumina, considering the Miled [26] model with spherical porosities whose size is equal to the one measured by SEM (approximately 1 μm in Fig. 7.b3) and a characteristic length l_c equal to three times the average grain size ($l_c = 1.44 \mu\text{m}$), the stress calculated by the model is 1144 MPa for a porosity rate of 20%, which is only 8% less than the average value obtained experimentally, apart from the dispersion of the results. Considering this model with isolated spherical pores of the same size as those in 20micro alumina, the calculated and measured fracture stress are close, confirming that pore geometry has little effect on the mechanical response at this scale. Pore size appears to be a first order parameter.

For 20meso alumina, the average pore size ϕ is around 33 μm so $\beta_m = 11.38 > 1$ considering as before $l_c = 2.43 \mu\text{m}$. Considering a population of a single size and the experimental fracture stress in compression equal to 1038 MPa, the equivalent pore size is only 4 μm . This value is of the order of the diameter of the smallest pores in 20meso alumina. If the model is suitable, it appears that the mechanical response may be driven by the smallest pores in the distribution rather than the largest. This seems to contradict the literature and observation of the fragments, where it has been shown that the largest pores are the crack initiation sites [42] or, at least, bridged by cracks (Fig. 15.b).

Moreover, the coefficient of variation ($\frac{\sigma_f}{\sigma_f}$) is greater for 20meso alumina (14%) than for 20micro (9%) while the fracture stress in compression is lower for 20meso. Isolated spherical porosity with a wide size distribution seems to increase the dispersion of mechanical results compared to interconnected porosity with a uniform size. This trend can be linked to the Weibull's probabilistic model, which is based on the assumption that the fracture is initiated by a single defect considered to be the most critical. In a way, this defect is the weakest link in the chain. In addition, as pore size increases, fracture stress in compression decreases. So the larger the pores, the more critical they are. Given that in 20meso alumina, it is possible to find very large pores (> 100 μm), these can lead to early fracture of the sample. This is why the scatter of experimental results is greater for 20meso alumina.

4.4. Effect of porosity and grain arrangement on the fracture mechanisms

SEM observations of the fracture surface of porous aluminas under quasi-static loading show that the fracture mechanisms involved during failure are highly dependent on the microstructure.

As the dense alumina is sintered at 1530 °C for 9 h, the grains coalesced strongly with each other allowing the grain boundaries to acquire maximum strength [40,67]. Therefore, the most efficient way for the crack propagation is to break the grains as evidenced by the cleavage zones and flat grains [34,68].

The failure of microporous alumina 20micro is mostly intergranular because the grain boundaries are weak. Indeed, given the sintering temperature and time ($t_s = 3 \text{ h}$, $T_s = 1400 \text{ °C}$) is lower than the theoretical temperature to obtain dense alumina ($t_s = 9 \text{ h}$, $T_s = 1530 \text{ °C}$), only the diffusion of atoms at the grain boundaries is activated and grains cannot coalesce significantly. At the end of this sintering, alumina can be described as a stack of polyhedral grains linked by their faces in which a network of pores passes [41,67,69]. Therefore, the grain boundaries do not acquire their ultimate strength. Thus, fracture mechanism minimising the fracture energy is the intergranular mode.

In contrast, for the same porosity rate, the 20meso alumina grains are more developed and have coalesced significantly due to the high sintering temperature (1530 °C) as for dense alumina. Moreover, the introduction of mesopores mathematically reduces the microporosity rate, resulting in a grain arrangement that is almost identical to that of dense alumina. The grain boundaries are stronger and the fracture mechanism minimising fracture energy is the transgranular mode as observed in Ji's fracture microscopies for fully dense alumina [34]. Furthermore, while the 20micro and 20meso aluminas have very different microstructures and fracture mechanisms, their mechanical properties (Young's modulus and fracture stress) are almost equivalent. This study of fracture surfaces reveals that the more compact the grain arrangement, the more the cracks will propagate in a transgranular way.

For the last grade of alumina (60meso), the polymeric network does not gel properly close to organic material (in this case pore-forming agents), resulting in poor quality sintering near the pores. As this grade is very porous and the pores are very close to each other, the grains did not sinter properly which results in weak grain boundaries. As for the 20micro grade, the energy minimising fracture mechanism is the intergranular mode.

5. Conclusions and perspectives

The present study investigates the effects of the rate and type of porosity on the mechanical behaviour and failure mechanisms of porous

alumina tested under quasi-static uniaxial compression. The conclusions are as follows:

1. As expected, the porosity has a strong influence on the mechanical response: the macroscopic mechanical properties (compressive strength/Young's modulus) decrease with increasing porosity and a transition from a elastic brittle to a quasi-brittle behaviour has been observed for porosity rates of around 60%.
2. On the other hand, at constant porosity, the macroscopic mechanical response is shown to depend on pore size but not on pore morphology. Applying Miled's model to the observed microstructures, the increase in compressive fracture stress between 20meso and 20micro alumina can be explained by the decrease in pore size. At isodensity, pore morphology has a limited effect on the mechanical response. Pore size appears to be a first order parameter. Furthermore, in the case of 20meso, by applying Miled's model, it appears that the mechanical response can be driven by the smallest pores in the distribution rather than the largest.
3. The fracture mechanisms also depend on the microstructure of the alumina:
 - For comparable pore morphologies (20meso/60meso), the higher the porosity, the more diffuse the damage throughout the sample. At low porosities, macrocracks propagate from pore to pore.
 - For equivalent porosity levels (20%), significant differences in grain scale microstructure lead to very different local fracture mechanisms despite similar mechanical response. A compact arrangement of grains leads to predominantly transgranular fracture, whereas a sparse arrangement leads to intergranular fracture.

This work has highlighted that the main observed differences induced by porosity are the fracture mechanisms. Adopted fracture test

Appendix A. Phenomenological model of Miled

Miled et al. [26] proposed a phenomenological model to predict the strength $\sigma(p, \phi)$ as a function of porosity rate p and porosity size ϕ considering spherical pores. This model has been confirmed with experimental data for porosity rates less than 50%. For example, an increase of pore size from 1 mm to 6.3 mm leads to a 44% reduction of the fracture stress in compression. The phenomenological model proposed by Miled is detailed in the annexe A. The model proposed by Miled [26] is detailed in the equations 8, varying between a lower limit $g_\infty(p)$ corresponding to brittle fracture behaviour, and an upper limit $g_0(p)$ corresponding to quasi-brittle behaviour:

$$\frac{\sigma(p, \Phi)}{\sigma_{matrix}} = \begin{cases} g_0(p) & \text{if } \beta_m \leq 1 \\ g_\infty(p) + \beta_m^{-1/3}(g_0(p) - g_\infty(p)) & \text{if } \beta_m \geq 1 \end{cases}$$

With

$$g_0(p) = \frac{0.41(1 - \frac{p}{p_{max}})}{0.41 + \frac{p}{p_{max}}}$$

$$g_\infty(p) = \frac{1 - \frac{p}{p_{max}}}{2(1 + 58.14 \frac{p}{p_{max}})}$$

And

$$\beta_m = \frac{\Phi}{l_c} \left(\frac{p}{p_{max}} - 1 \right) \left(\frac{5}{3} \left(\frac{p}{p_{max}} \right)^2 - \frac{p}{p_{max}} - 1 \right)$$

σ_{matrix} is the fracture stress in compression of constitutive material and p_{max} is the compactness of a face centered cubic FCC arrangement which can be assimilated to the maximum porosity rates achievable with **spherical pores** of a single size. β_m is called "brittleness mesoscopic number" and characterized the brittleness of the fracture. The greater β_m , the more brittle the ceramic failure mode.

References

[1] M.V Staub, Étude du comportement mécanique à rupture des aluminés de forte porosité: Application aux supports de catalyseurs d'hydrotraitement des résidus, page 198.

could be used to study more precisely the influence of porosities on crack propagation. A knowledge of the microstructure of each sample established by X-ray microtomography before testing would provide an in-depth explanation of the influence of the pores (size and shape) on the failure mechanisms.

CRediT authorship contribution statement

HENRY Quentin: Data acquisition (microstructural observation, mechanical characterisation), Methodology, Writing - original draft, Writing - review and editing. **VIOT Philippe:** Scientific support, Supervision, Validation, Funding acquisition, Writing support. **LE BARBENCHON Louise:** Scientific support (microstructural observation), Supervision, Validation, Writing support. **COSCULLUELA Antonio:** Funding acquisition, Supervision, Validation. **KOPP Jean-Benoit:** Scientific support, Funding acquisition, Supervision, Validation, Writing support.

Declaration of Competing Interest

The authors declare that they have no known competing financial interests or personal relationships that could have appeared to influence the work reported in this paper.

Acknowledgments

We would like to thank the Nouvelle-Aquitaine region and the CEA for funding this research (CERAMOD²) and the company Galtenco solution for the supply of materials. Furthermore, we would like to thank J.

Malvestio (PLACAMAT institute, Talence) for his help during in situ X-ray tomography.

[2] T. Noda. Advanced sic-sic composites for nuclear application. *Handbook of Advanced Ceramics and Composites: Defense, Security, Aerospace and Energy Applications*, pages 641–666, 2020.

[3] M. Amaral, M.A. Lopes, R.F. Silva, J.D. Santos, *Densification route and mechanical properties of si3n4-bioglass biocomposites*, *Biomaterials* 23 (3) (2002) 857–862.

- [4] S. Samavedi, A.R. Whittington, A.S. Goldstein, Calcium phosphate ceramics in bone tissue engineering: a review of properties and their influence on cell behavior, *Acta Biomater.* 9 (9) (2013) 8037–8045.
- [5] *The Ceramic Society of Japan. Advanced Ceramic Technologies & Products.* Springer Science & Business Media, 2012.
- [6] E. Medvedovski, Ballistic performance of armour ceramics: Influence of design and structure, part 1, *Ceram. Int.* 36 (7) (2010) 2103–2115.
- [7] E. Medvedovski, Ballistic performance of armour ceramics: Influence of design and structure, Part 2, *Ceram. Int.* 36 (7) (2010) 2117–2127.
- [8] S. Vijayan, P. Wilson, K. Prabhakaran, Processing of ceramic foams for thermal protection, *Handb. Adv. Ceram. Compos.: Def., Secur., Aersp. Energy Appl.* (2020) 1105–1134.
- [9] N. Muhammad, R. Sinha, E.R. Krishnan, C.L. Patterson, Ceramic filter for small system drinking water treatment: evaluation of membrane pore size and importance of integrity monitoring, *J. Environ. Eng.* 135 (11) (2009) 1181–1191.
- [10] D. Buncianu, N. Tessier-Doyen, J. Absi, R. Negru, D.A. Serban, L. Marşavin, Multi-scale mechanical behaviour of a highly porous alumina based foam, *Met. Mater. Int.* 26 (10) (2020) 1524–1532.
- [11] B.S.M. Seeber, U.T. Gonzenbach, L.J. Gauckler, Mechanical properties of highly porous alumina foams, *J. Mater. Res.* 28 (17) (2013) 2281–2287.
- [12] R.L. Coble, W.D. Kingery, Effect of porosity on physical properties of sintered alumina, *J. Am. Ceram. Soc.* 39 (11) (1956) 377–385.
- [13] F.P. Knudsen, Effect of porosity on young's modulus of alumina, *J. Am. Ceram. Soc.* 45 (2) (1962) 94–95.
- [14] J.C. Wang, Young's modulus of porous materials. ii: Young's modulus of porous alumina with changing pore structure, *J. Mater. Sci.* 19 (3) (1984) 809–814.
- [15] R.W. Rice, Evaluation and extension of physical porosity-porosity models based on minimum solid area, *J. Mater. Sci.* 31 (1996) 102–118.
- [16] Aldo R. Boccaccini, Zhongyun Fan, A new approach for the young's modulus-porosity correlation of ceramic materials, *Ceram. Int.* 23 (3) (1997) 239–245.
- [17] W. Pabst, T. Uhlířová, E. Gregorová, A. Wiegmann, Young's modulus and thermal conductivity of closed-cell, open-cell and inverse ceramic foams—model-based predictions, cross-property predictions and numerical calculations, *J. Eur. Ceram. Soc.* 38 (6) (2018) 2570–2578.
- [18] E. Ryskhewitch, Compression strength of porous sintered alumina and zirconia: 9th communication to ceramography, *J. Am. Ceram. Soc.* 36 (2) (1953) 65–68.
- [19] F.P. Knudsen, Dependence of mechanical strength of brittle polycrystalline specimens on porosity and grain size, *J. Am. Ceram. Soc.* 42 (8) (1959) 376–387.
- [20] Y. Kwan, D.J. Stephenson, J.R. Alcock, The porosity dependence of flexural modulus and strength for capsule-free hot isostatically pressed porous alumina, *J. Mater. Sci.* 35 (2000) 1205–1211.
- [21] F. Tancret, G. Desgardin, F. Osterstock, Influence of porosity on the mechanical properties of cold isostatically pressed and sintered $\text{YBa}_2\text{Cu}_3\text{O}_{7-x}$ superconductors, *Philos. Mag.* A 75 (2) (1997) 505–523.
- [22] D.P.H. Hasselman R.M. Fulrath. *Eff. Cylind. porosity young's Modul. Polycryst. brittle Mater.* 1965.
- [23] Dean-Mo Liu, Influence of porosity and pore size on the compressive strength of porous hydroxyapatite ceramic, *Ceram. Int.* 23 (2) (1997) 135–139.
- [24] K. Yoshida, H. Tsukidate, A. Murakami, H. Miyata, Influence of pore size on fracture strength of porous ceramics, *J. Solid Mech. Mater. Eng.* 2 (8) (2008) 1060–1069.
- [25] S. Meille, M. Lombardi, J. Chevalier, L. Montanaro, Mechanical properties of porous ceramics in compression: On the transition between elastic, brittle, and cellular behavior, *J. Eur. Ceram. Soc.* 32 (15) (2012) 3959–3967.
- [26] K. Miled, K. Sab, R. Le Roy, Particle size effect on eps lightweight concrete compressive strength: Experimental investigation and modelling, *Mech. Mater.* 39 (3) (2007) 222–240.
- [27] Anthony P. Roberts, Edward J. Garboeci, Elastic properties of model porous ceramics, *J. Am. Ceram. Soc.* 83 (12) (2000) 3041–3048.
- [28] J. Luo, R. Stevens, Porosity-dependence of elastic moduli and hardness of 3y-tzp ceramics, *Ceram. Int.* 25 (3) (1999) 281–286.
- [29] AV Manoylov, Feodor M Borodich, Henry Peredur Evans, Modelling of elastic properties of sintered porous materials, 20120689, *Proc. R. Soc. A: Math., Phys. Eng. Sci.* 469 (2154) (2013), 20120689.
- [30] A.S. Vavakin, R.L. Salganik, Effective characteristics of nonhomogeneous media with isolated inhomogeneities, *Mech. Solids* 10 (1975) 58–66.
- [31] A.S. Vavakin, R.L. Salganik, Effective elastic properties of bodies with isolated cracks, cavities, and rigid inhomogeneities, *Akad. Nauk SSSR* (1978) 95–107.
- [32] C.G. Sammis, M.F. Ashby, The failure of brittle porous solids under compressive stress states, *Acta Metall.* 34 (3) (1986) 511–526.
- [33] Vinit Vijay, Deshpande and Romana Plat. Compression failure of porous ceramics: a computational study about the effect of volume fraction on damage evolution and failure, *Mech. Mater.* 177 (2023) 104533.
- [34] M. Ji, H. Li, J. Zheng, S. Yang, Z. Zaiemeyek, J.D. Hogan, An experimental study on the strain-rate-dependent compressive and tensile response of an alumina ceramic, *Ceram. Int.* 48 (19) (2022) 28121–28134.
- [35] James Lankford, Compressive strength and microplasticity in polycrystalline alumina, *J. Mater. Sci.* 12 (1977) 791–796.
- [36] A.C. Young, O.O. Omatete, M.A. Janney, P.A. Menchhofer, Gelcasting of alumina, *J. Am. Ceram. Soc.* 74 (3) (1991) 612–618.
- [37] Y. Zhang, J. Xu, Y. Qu, X. Xi, J. Yang, Gelcasting of alumina suspension using gellan gum as gelling agent, *Ceram. Int.* 40 (4) (2014) 5715–5721.
- [38] X. Mao, S. Shimai, M. Dong, S. Wang, Gelcasting of alumina using epoxy resin as a gelling agent, *J. Am. Ceram. Soc.* 90 (3) (2007) 986–988.
- [39] M. Potoczek, Gelcasting of alumina foams using agarose solutions, *Ceram. Int.* 34 (3) (2008) 661–667.
- [40] A. Ndayishimiye. *Sur un nouveau procédé de frittage de céramiques à basse température: le frittage hydrothermal. Développement et approche mécanistique.* PhD thesis, Université de Bordeaux, 2017.
- [41] B. Suleiman, H. Zhang, Y. Ding, Y. Li, Microstructure and mechanical properties of cold sintered porous alumina ceramics, *Ceram. Int.* 48 (10) (2022) 13531–13540.
- [42] R.W. Rice, Pores as fracture origins in ceramics, *J. Mater. Sci.* 19 (1984) 895–914.
- [43] L. Le Barbençon. *Description multi-échelles du comportement mécanique d'un matériau cellulaire composite sous sollicitations sévères. Application aux agglomérés de liège pour l'aéronautique.* PhD thesis, HESAM Université, 2020.
- [44] H. Wadell, Volume, shape, and roundness of quartz particles, *J. Geol.* 43 (3) (1935) 250–280.
- [45] ASTM C1424. Standard test method for monotonic compressive strength of advanced ceramics at ambient temperature. Technical report 2019.
- [46] I.S.O. Iso 17162 - fine ceramics (advanced ceramics, advanced technical ceramics) — mechanical properties of monolithic ceramics at room temperature — determination of compressive strength. Technical report, 2014.
- [47] N.L. Savchenko, T.Y. Sablina, L.N. Sevostyanova, S.P. Buyakova, S.N. Kulkov, Deformation and fracture of porous brittle materials under different loading schemes, *Russ. Phys. J.* 58 (2016) 1544–1548.
- [48] NF EN 623-3. *Céramiques monolithiques — propriétés générales et texturales: Partie 3: Détermination de la taille des grains et de la distribution granulométrique.* Technical report, 2002.
- [49] R.M. German. *Sintering theory and practice.* 1996.
- [50] J. Lamon, La rupture des céramiques, *Rev. De Métallurgie* 92 (2) (1995) 265–284.
- [51] M.F. Ashby, C.G. Sammis, The damage mechanics of brittle solids in compression, *Pure Appl. Geophys.* 133 (1990) 489–521.
- [52] R.M. Brannon, M.Y. Lee, and D.R. Bronowski. Uniaxial and triaxial compression tests of silicon carbide ceramics under quasi-static loading condition. Technical report, Sandia National Laboratories (SNL), Albuquerque, NM, and Livermore, CA., 2005.
- [53] K.K. Phani, S.K. Niyogi, Young's modulus of porous brittle solids, *J. Mater. Sci.* 22 (1) (1987) 257–263.
- [54] M.V. Grigoriev, V.I. Kashirina, and S.N. Kulkov. Fracture peculiarities of porous alumina metamaterial. page 020117, Tomsk, Russia, 2019.
- [55] W. Pabst, E. Gregorová, G. Tichá, Elasticity of porous ceramics—a critical study of modulus-porosity relations, *J. Eur. Ceram. Soc.* 26 (7) (2006) 1085–1097.
- [56] Z. Živcová, M. Cerný, W. Pabst, E. Gregorová, Elastic properties of porous oxide ceramics prepared using starch as a pore-forming agent, *J. Eur. Ceram. Soc.* 29 (13) (2009) 2765–2771.
- [57] Z. Hashin, S. Shtrikman, A variational approach to the theory of the elastic behaviour of multiphase materials, *J. Mech. Phys. Solids* 11 (2) (1963) 127–140.
- [58] W. Pabst and E. Gregorová. Young's modulus of isotropic porous materials with spherical pores. *Journal of the European Ceramic Society*, 34(13):3195–3207, 2014.
- [59] L.J. Gibson, Cellular solids, *Mrs Bull.* 28 (4) (2003) 270–274.
- [60] L.J. Gibson, M.F. Ashby, G.S. Schajer, C.I. Robertson, The mechanics of two-dimensional cellular materials, *Proc. R. Soc. Lond. A. Math. Phys. Sci.* 382 (1782) (1982) 25–42.
- [61] S.C. Carniglia, Reexamination of experimental strength-vs-grain-size data for ceramics, *J. Am. Ceram. Soc.* 55 (5) (1972) 243–249.
- [62] N.J. Petch, The cleavage strength of polycrystals, *J. Iron Steel Inst.* 174 (1953) 25–28.
- [63] A. Zimmermann, M. Hoffman, B.D. Flinn, R.K. Bordia, T. Chuang, Edwin R.F. Jr., and J. Rödel. Fracture of alumina with controlled pores. *Journal of the American Ceramic Society*, 81(9):2449–2457, 1998.
- [64] A.S. Wagh, R.B. Poepel, J.P. Singh, Open pore description of mechanical properties of ceramics, *J. Mater. Sci.* 26 (1991) 3862–3868.
- [65] A.A. Griffith, Vi. the phenomena of rupture and flow in solids, *Philos. Trans. R. Soc. Lond. Ser. A, Contain. Pap. A Math. Or Phys. Character* 221 (582-593) (1921) 163–198.
- [66] C. Bartuli, E. Bemporad, J.M. Tulliani, J. Tirillò, G. Pulci, M. Sebastiani, Mechanical properties of cellular ceramics obtained by gel casting: Characterization and modeling, *J. Eur. Ceram. Soc.* 29 (14) (2009) 2979–2989.
- [67] R.L. Coble, Sintering crystalline solids. i. intermediate and final state diffusion models, *J. Appl. Phys.* 32 (5) (1961) 787–792.
- [68] S.J. Chantikul, P. Bennisson, B.R. Lawn, Role of grain size in the strength and r-curve properties of alumina, *J. Am. Ceram. Soc.* 73 (8) (1990) 2419–2427.
- [69] R.L. Coble. Sintering crystalline solids. ii. experimental test of diffusion models in powder compacts. *Journal of applied physics*, 32(5):793–799, 1961.